Supplementary Information

Low-temperature Highly Selective Kolbe Electrolysis of Acetic Acid in Bio-oil on a Stable *In-Situ* Grown RuO_2/TiO_2 at Industrial-level Current

Yangxin Jin[1,2], Shengqin Liu[1,2], Zhe Wang[1], Qi Zhu[1,2], Qingguo Le[1,2], Shan Shao[1,2], Sam H.-Y. Hsu[1,3], Anqing Zheng[5], Jun Zhao[4], Jason Chun-Ho Lam[1,2*]

[1]*School of Energy and Environment, City University of Hong Kong, Kowloon Tong, Hong Kong SAR, China.*
[2]*State Key Laboratory of Marine Pollution (SKLMP), City University of Hong Kong, Kowloon Tong, Hong Kong SAR, China.*
[3]*Department of Materials Science and Engineering, City University of Hong Kong, Kowloon Tong, Hong Kong SAR, China.*
[4]*Department of Biology, Institute of Bioresource and Agriculture, Hong Kong Baptist University, Hong Kong SAR, China.*
[5]*CAS Key Laboratory of Renewable Energy, Guangzhou Institute of Energy Conversion, Chinese Academy of Sciences, Guangzhou, China.*

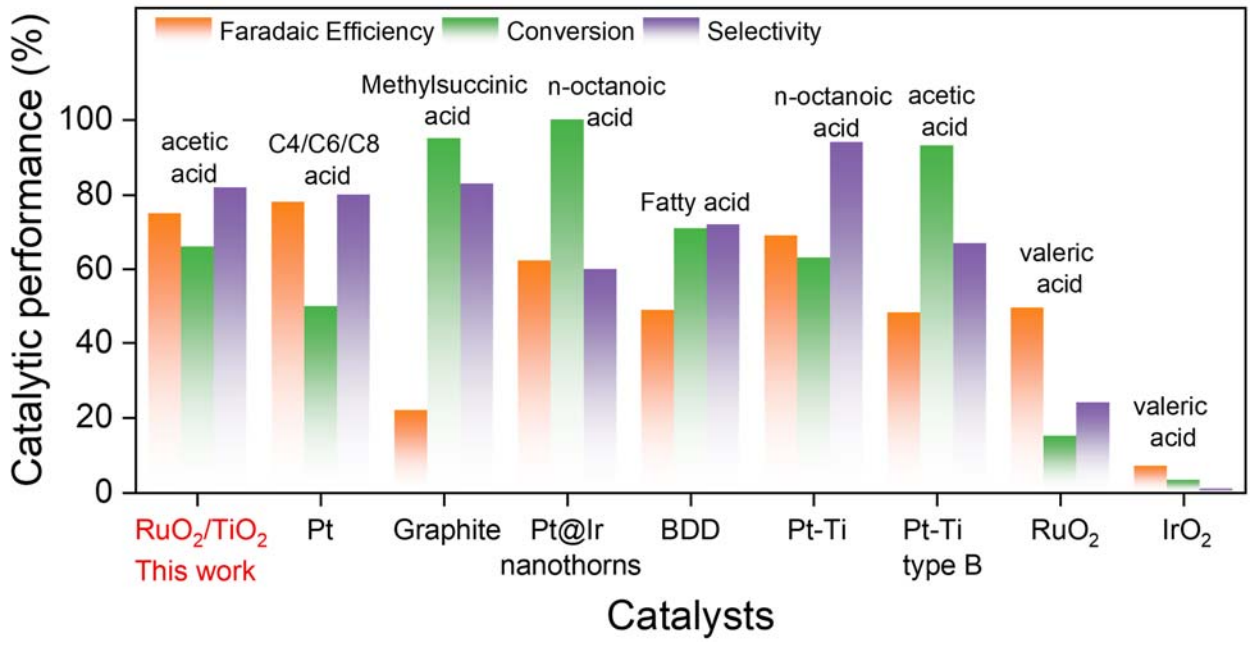

Fig. S1. Catalytic performance comparison of the state-of-the-art catalysts that applied in KBE.

Table S1. Comparison of various applied anode materials that applied in KBE

Entry	Anode	Optimized condition	FE (%)	Conv. (%)	Sel. (%)	Stability	Ref.
1	RuO_2/TiO_2 (This	150 mA cm^{-2}, ~1.0 M Acetic Acid, pH 4.6, 5℃	~75	66	82	> 150 h	-
2	Pt	3 V vs. Ag/AgCl, 70-80 mA cm^{-2}, ~1.0 M C4/C6/C8, pH 9-9.5	78.1	25-50	20-80	5~6 h	[1]
3	Multiscale structural	30 wt% Stearic acid, 80℃, 10V	-	-	-	> 8.3 h	[2]
4	Graphite	0.8 M Methylsuccinic acid, pH 5.7, 60℃, 95	22	>95	83	3 h	[3]
5	Pt@Ir Nanothorn	0.5 M n-octanoic acid, pH 14, 250 mA cm^{-2},	62.3	~100	> 60	5 cycles	[4]
6	Pt-Ti (Platinized Titanium)	1.0 M Fatty acid, pH 6.2, 30-72℃, 300 mA cm^{-2}	24-53	50-71	48-80	-	[5]
7	BDD	1.0 M Fatty acid, pH6.2, 30-72℃, 300 mA cm^{-2}	45-49	52-71	66-72	-	[5]
8	Pt-Ti (Platinized Titanium	1.0 M n-octanoic acid, pH 10-10.5, 480 mA cm^{-2}, 20 ℃	69	63	92-94	~4 h	[6]
9	Pt-Ti (Type B)	1.0 M Acetic acid, pH 7.0, 150 mA cm^{-2}	48.3	93.1	66.9	~10000 h	[7]
10	Carbon electrode	1 wt% Acetic acid, 10–30 °C, 29V	0.7-2.3	11.8	21	8 h	[8]
11	RuO_2 nanopartic	0.5 M valeric acid, 4.5 V vs. RHE, pH 6.0, 0℃	85.4	-	31.3	6 h	[9]
12	RuO_2 thin films	0.5M valeric acid, pH 5, 15-	49.7	15.2	24.1	-	[10]
13	IrO_2 thin films	0.5M valeric acid, pH 5, 15-20 °C, 50 mA cm^{-2}	7.1	3.4	0	-	[10]

Note: Not all the stability measurement of these reported materials has been invertigated in their work.

By comparing recent related studies on Kolbe electrolysis since 2010, we found that platinum-based materials are still the main anode materials used and the catalytic performance (based on Faraday efficiency, selectivity and conversion) is relatively stable, carbon-based materials such as graphite and BDD also exhibit promising applications, and the catalytic performance of metal oxides such as RuO_2 and IrO_2 still needs to be improved. Unfortunately, most of the research work has not paid much attention to the stability of the catalysts, so no comparison is made here.

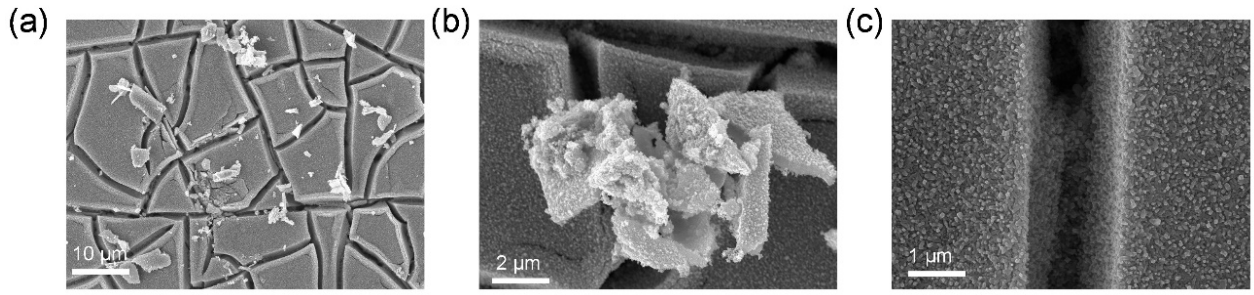

Fig. S2. SEM images of the RuO_2/TiO_2 electrode.

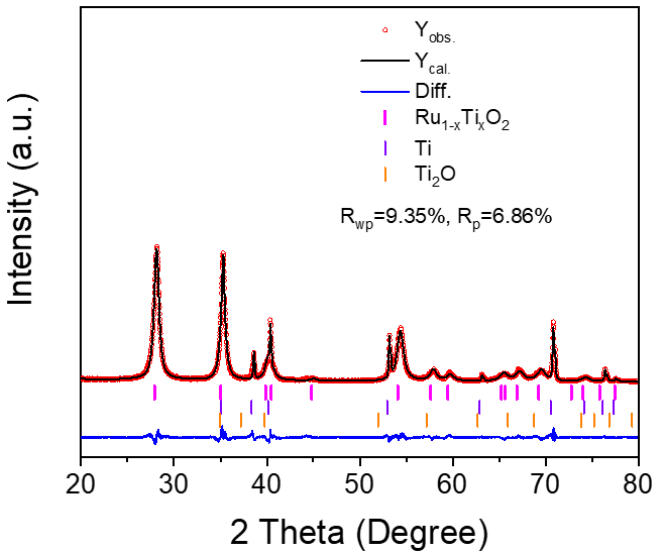

Fig. S3. XRD pattern and fitting analysis of the RuO_2/TiO_2 electrode surface. $Y_{obs.}$ is the obtained experimental value, $Y_{cal.}$ is the calculated value, the blue line indicates the difference between the $Y_{obs.}$ and $Y_{cal.}$, and the vertical dashes of different colors indicate the Bragg's position.

Table S2. The Rietveld refinement results of RuO_2/TiO_2

Chemical formula		$Ru_{0.971}Ti_{0.029}O_2$	Ti	Ti_2O
Relative content %		65.93	32.88	1.18
Space group		P42/mnm	P63/mmc	P-3m1
Cell parameters	a (Å)	4.52084 (50)	2.95202(34)	2.96176
	b (Å)	4.52084 (50)	2.95202(34)	2.96176
	c (Å)	3.10645 (50)	4.68948(51)	4.8301
	α (°)	90	90	90
	β (°)	90	90	90
	γ (°)	90	120	120
	Volume ($Å^3$)	63.490(17)	35.3910(90)	36.693
Fitting index		R_{wp}= 9.35% R_p= 6.86%	GOF= 1.73	χ^2=2.99

R_p: Profile R factor, R_{wp}: Weighted R factor, χ^2: Goodness factor. The Rietveld refinement analysis is a typical technique described by Hugo Rietveld for the application during the characterization of crystalline materials. In the case, the values of R_{wp} factor is lower than 10% which confirm the suitable peaks fitting and convincing refinement.[11]

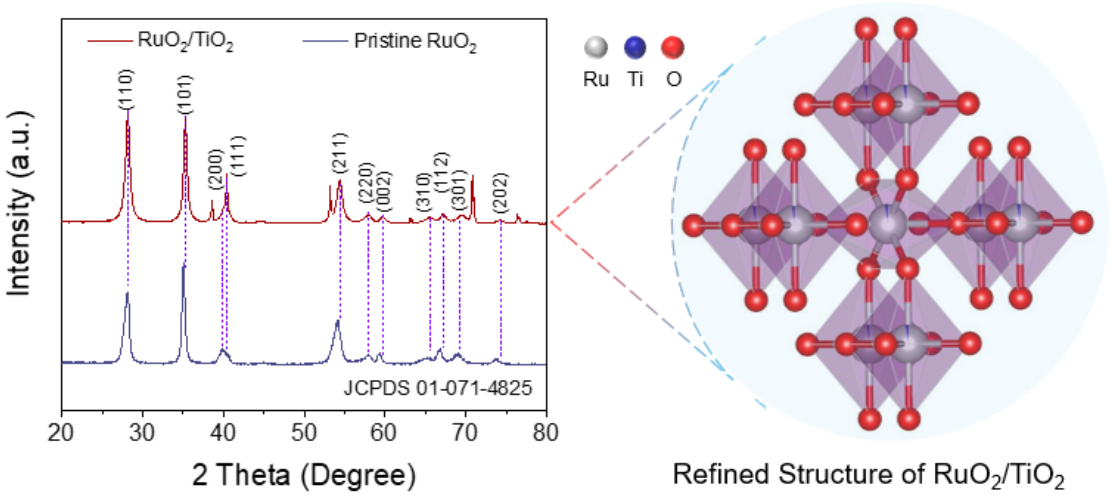

Fig. S4. The XRD patterns of RuO_2/TiO_2 and pristine RuO_2, and the refined structure of RuO_2/TiO_2.

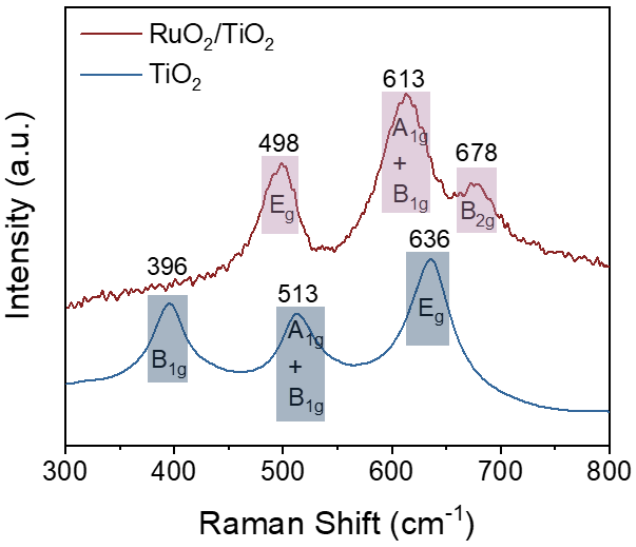

Fig. S5. Raman spectra of RuO_2/TiO_2 and calcinated Ti (TiO_2).

Table S3. Binding energy of the Ru, Ti, O in the characterized materials.

Catalysts	Binding energy of Ti (eV)		Binding energy of Ru (eV)				Binding energy of O (eV)		
	2p 3/2	2p 1/2	3p 3/2 (Sat)	3p 1/2 (Sat)	3d 5/2 (Sat)	3d 3/2 (Sat)	Ti (Ru)O_2	Ads. OH	Ads. H_2O
Calcinated Ti sheet (TiO_2)	458.6	464.3	/	/	/	/	529.7 (39.2 %)	531.0 (59.0 %)	532.8 (1.8%)
RuO_2/TiO_2	458.2	463.8	462.0 (464.3)	484.4 (487.5)	280.5 (282.2)	284.7 (286.4)	529.0 (49.1 %)	530.1 (24.3 %)	531.6 (26.6 %)
Pristine RuO_2	/	/	462.3 (464.3)	484.7 (487.8)	280.7 (282.3)	284.9 (286.6)	529.2 (42.1 %)	530.2 (25.8 %)	531.7 (32.1 %)

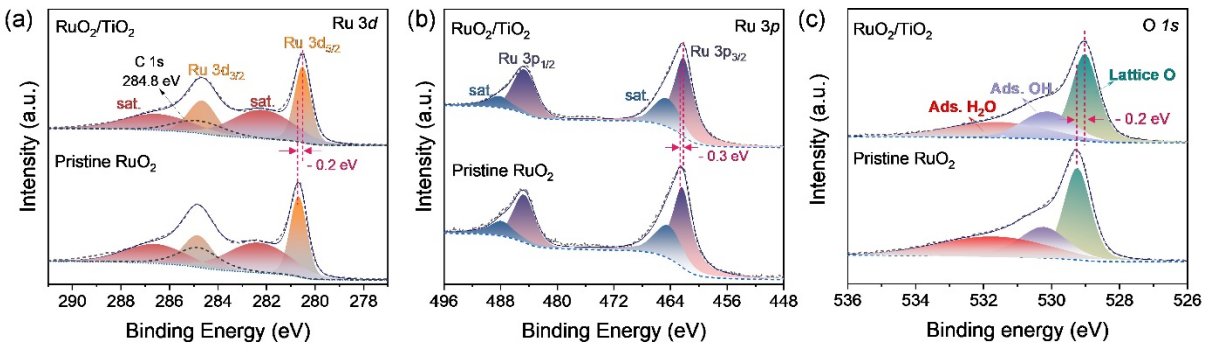

Fig. S6. High resolution spectra of (a) Ru 3d, (b) Ru 3p and (c) O 1s in pristine RuO_2 and synthesized RuO_2/TiO_2.

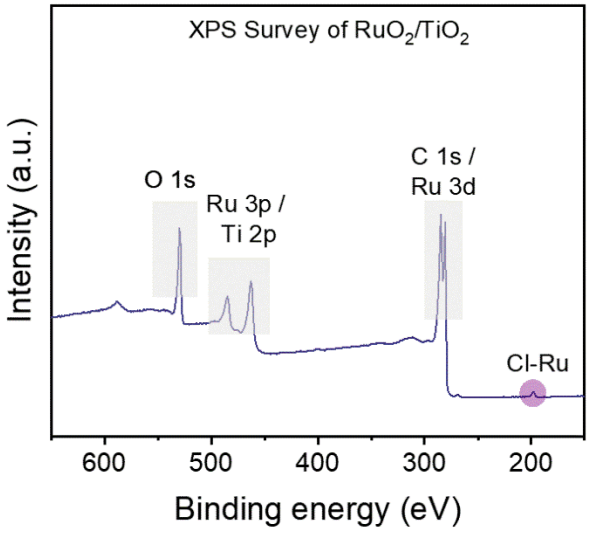

Fig. S7. XPS scan survey of RuO_2/TiO_2.

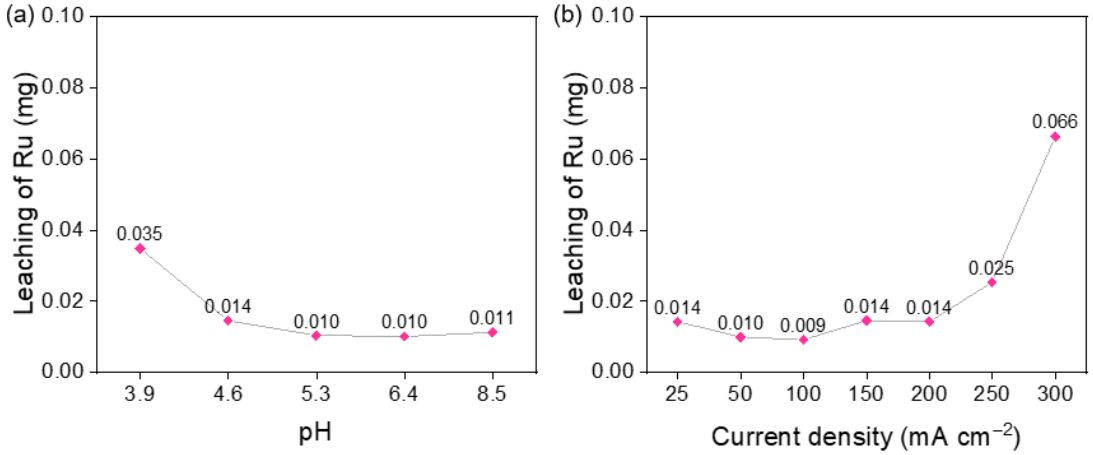

Fig. S8. ICP analysis of the solution after KBE in different pH (a) and current densities (b).

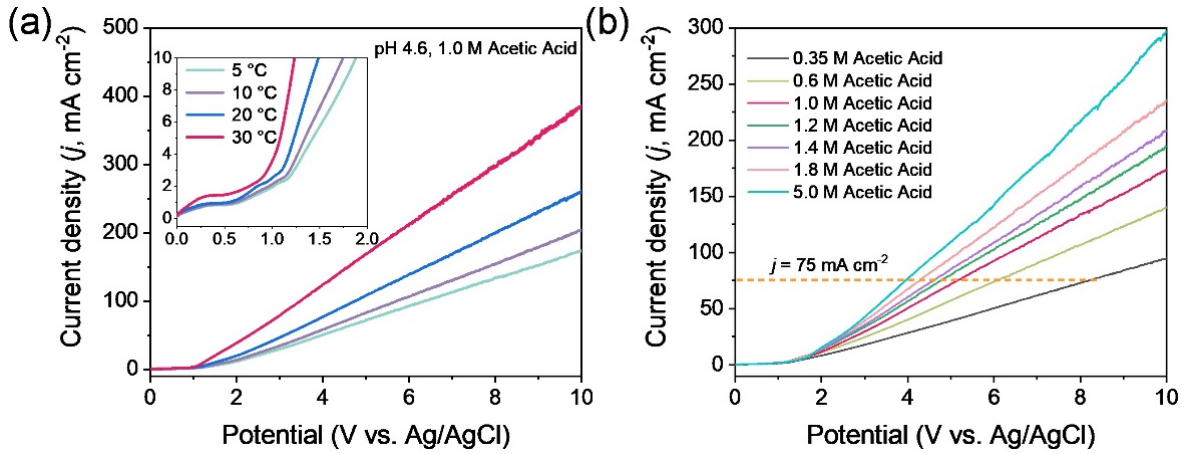

Fig. S9. (a) LSV curves of RuO_2/TiO_2 at different temperature. (b) LSV curves of RuO_2/TiO_2 in various concentration of acetic acid at 5 ℃. LSVs are recorded with scan rate of 50 mV/s at stirring speed of 900 rpm.

Table S4. Specifications of the electrolyte properties used in the LSV studies and the KBE experiments.

Solution condition	CH_3COOH (mol/L)	$NaCH_3COO$ (mol/L)	Conductivity (ms)	Initial pH	pH after KBE
0.35M Acetic Acid electrolyte	0.175	0.175	13.7	4.6	8.9
0.6M Acetic Acid electrolyte	0.3	0.3	19.5	4.6	9.1
1.0M Acetic Acid electrolyte @150mA cm^{-2}	0.2	0.8	42.5	5.3	10.0
1.0M Acetic Acid electrolyte @150mA cm^{-2}	0.82	0.18	12.2	3.9	4.8
1.0M Acetic Acid electrolyte @150mA cm^{-2}	-	1.0	49.9	8.3	9.2
1.0M Acetic Acid electrolyte @150mA cm^{-2}	0.5	0.5	30.7	4.6	9.3
1.2M Acetic Acid electrolyte @150mA cm^{-2}	0.6	0.6	33.7	4.6	9.1
1.4M Acetic Acid electrolyte @150mA cm^{-2}	0.7	0.7	36.9	4.6	9.3
1.8M Acetic Acid electrolyte @150mA cm^{-2}	0.9	0.9	45.7	4.6	9.5
1.0M Acetic Acid electrolyte @150mA cm^{-2}	0.02	0.98	51.7	6.4	9.1
Crude Bio-oil	~1.4	-	1.3	2.3~2.4	-
1.5M AA	1.5	-	1.2	2.4	-
~1.5M aqueous-extracted bio-oil @150mA cm^{-2}	~0.7	~0.7	35.1	4.2	8.9

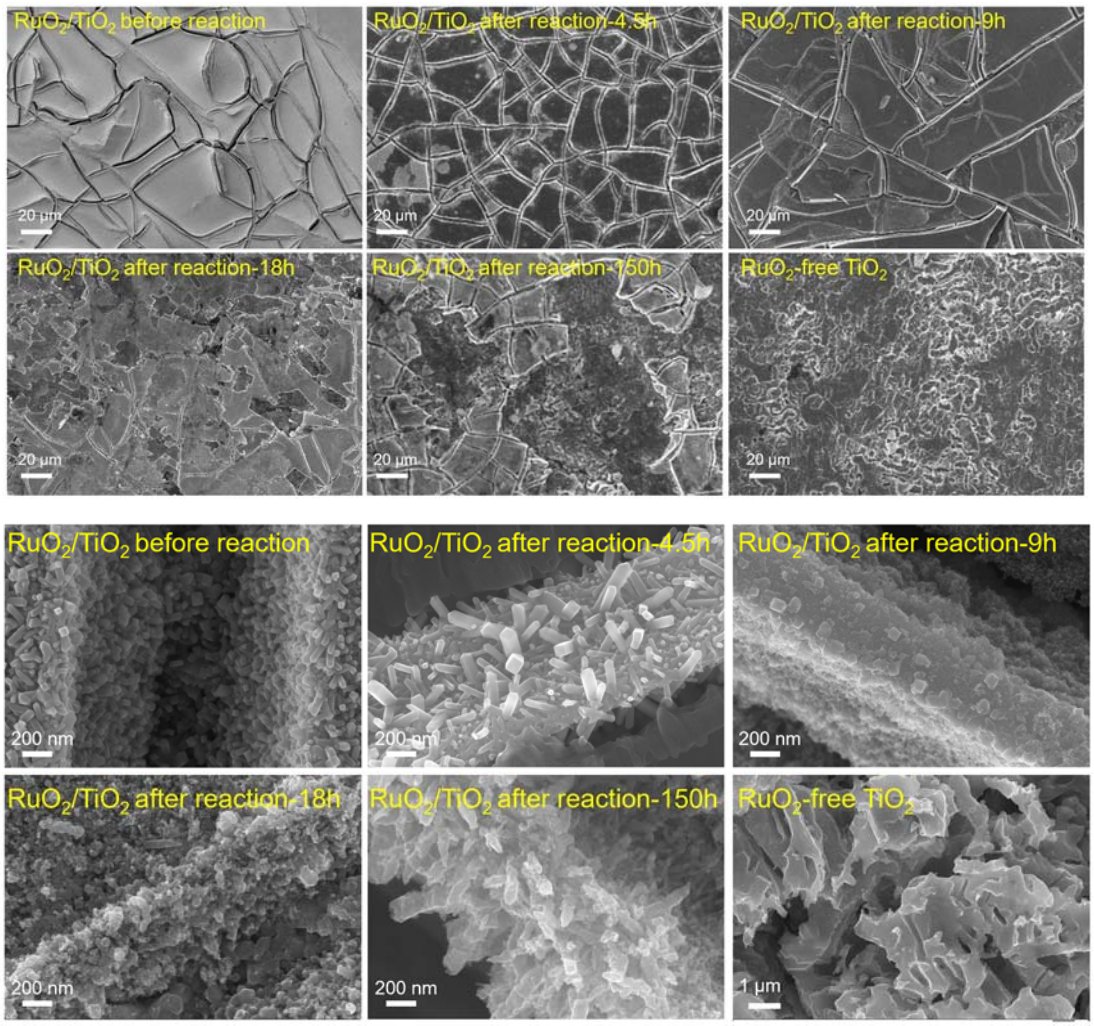

Fig. S10. SEM images of the RuO_2/TiO_2 electrode before reaction, after different reaction duration (4.5h, 9h, 18h and 150h) and RuO_2-free TiO_2.

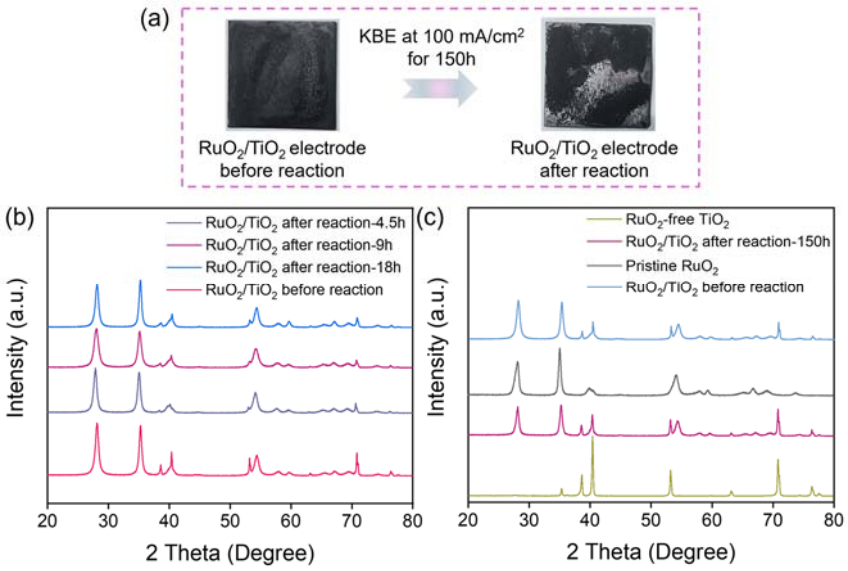

Fig. S11. (a) Comparison of the RuO_2/TiO_2 electrode before and after reaction. (b-c) XRD patterns of the RuO_2/TiO_2 electrodes before and after different reaction durations (4.5h, 9h, 18h, 150h).

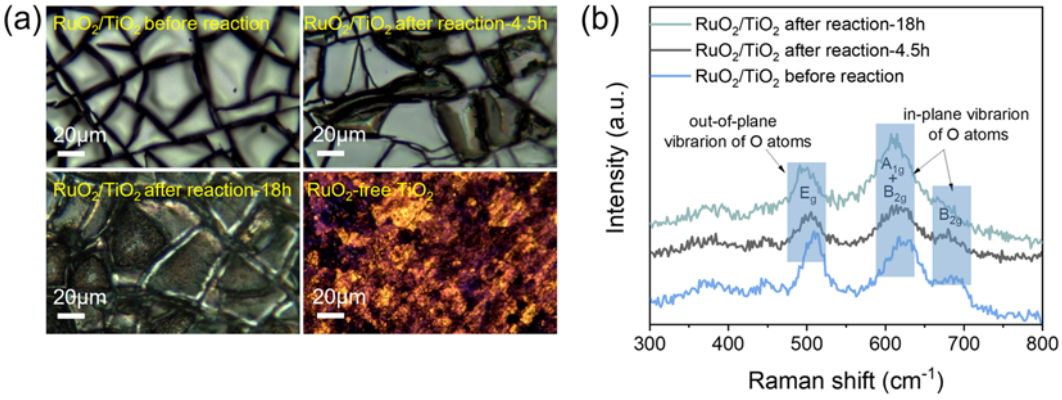

Fig. S12. (a) Comparison of the RuO_2/TiO_2 electrode and TiO_2 surface by Raman-photo before and after reaction. (b) Raman spectra of the RuO_2/TiO_2 electrodes before and after different reaction durations (4.5h, 18h).

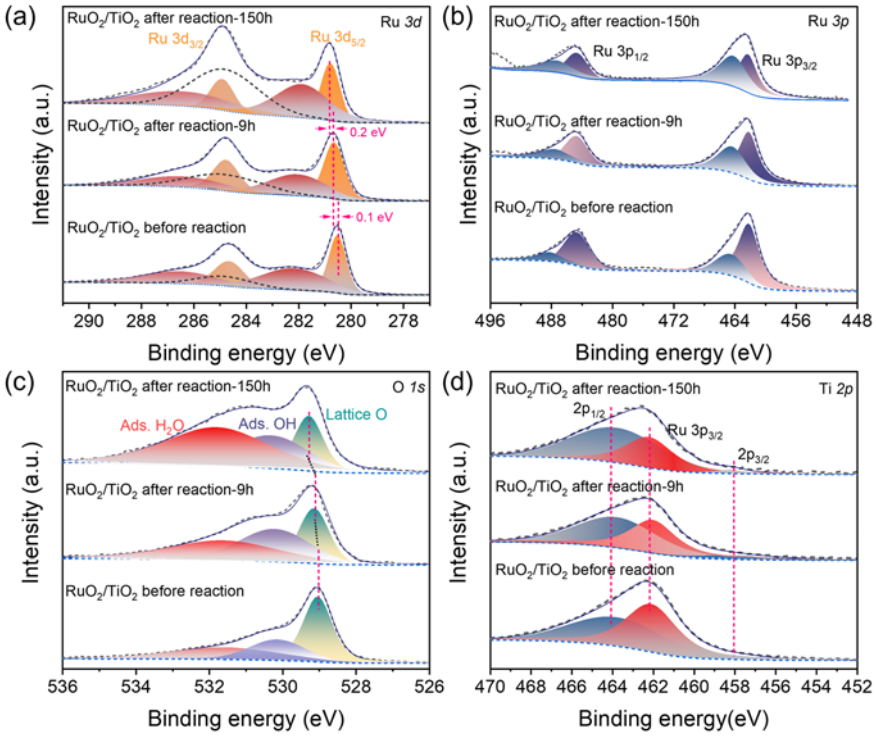

Fig. S13. XPS spectra of (a) Ru 3d, (b) Ru 3p, (c) O 1s and Ti 2p in pristine synthesized RuO_2/TiO_2 before and after reaction.

Table S5. Binding energy of the Ru, Ti, O in the characterized materials.

Catalysts	Binding energy of Ti		Binding energy of Ru (eV)				Binding energy of O (eV)		
	2p 3/2	2p 1/2	3p 3/2 (Sat)	2p 1/2 (Sat)	3d 5/2 (Sat)	3d 3/2 (Sat)	Ti (Ru)O_2	Ads. OH	Ads. H_2O
RuO_2/TiO_2 before	458.2	463.8	462.0 (464.3)	484.4 (487.5)	280.5 (282.2	284.7 (286.4	529.0 (49.1%)	530.1 (24.3%)	531.6 (26.6%
RuO_2/TiO_2 after reaction-9h	458.2	463.8	462.1 (464.3)	484.7 (487.5)	280.7 (282.1)	284.8 (286.5)	529.1 (27.3%)	530.2 (35.1%)	531.6 (37.6%)
RuO_2/TiO_2 after reaction-	458.2	463.8	462.2 (464.1)	484.6 (487.3)	280.8 (281.9)	284.9 (286.4)	529.3 (20.6%)	530.3 (28.0%)	531.8 (51.4%)

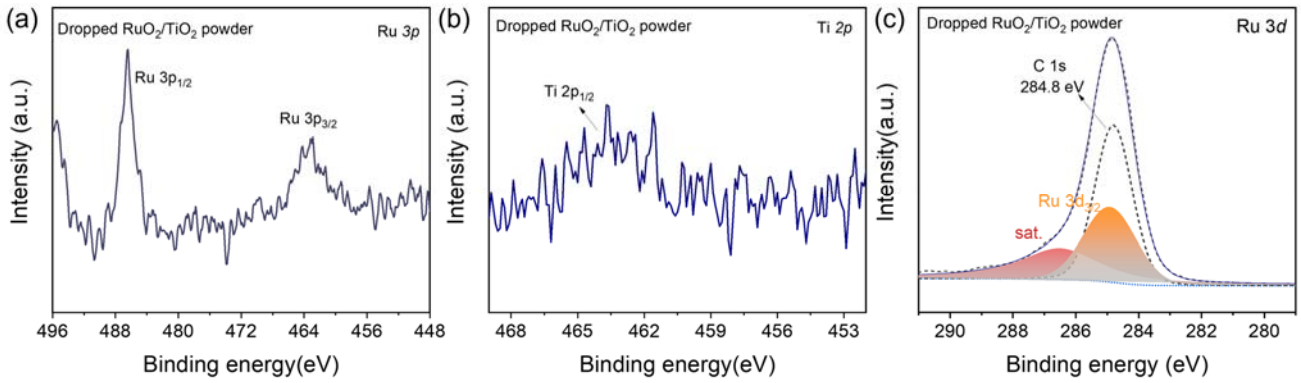

Fig. S14. XPS spectra of (a) Ru 3p, (b) Ti 2p and (c) Ru 3d in the dropped RuO_2/TiO_2 powder after reaction.

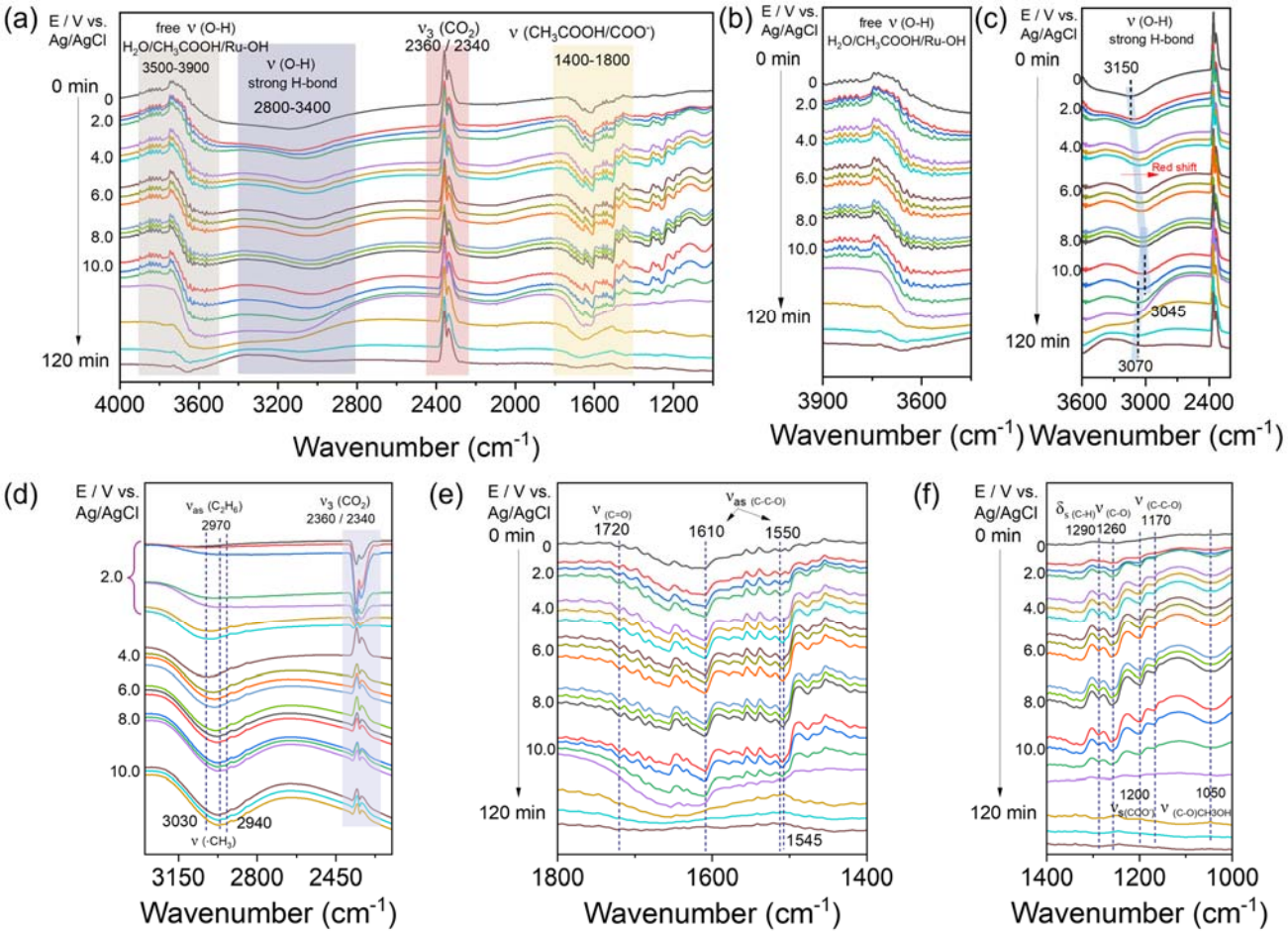

Fig. S15. *In-situ* electrochemical ATR-FTIR spectra. (a) Selected *in-situ* ATR-FTIR spectra of Kolbe electrolysis of AA over RuO_2/TiO_2 based on stepwise switching the potential from 0 V to −10 V (vs. Ag/AgCl). (b, c, e, f) Comparison of different region with the change of potential and time. (d) Differential spectrum analysis.

The Kolbe electrolysis of acetic acid can be divided into three steps: Step 1 is the dissociation of acetic acid to yield an acetate anion. Step 2 is the oxidative electrolysis of carboxyl group, which oxidize the acetate anion to acetate radical. The carboxyl radical can rearrange to liberate a CO2, breaking the internal C-C bond and leave behind a methyl radical ($\cdot CH_3$). Step 3 is the coupling of $\cdot CH_3$ to form ethane (C_2H_6). To investigate the reaction mechanism, *in-situ* ATR-FTIR was applied to monitor the reaction process by switching potentials.

$$Step\ 1: CH_3COOH \rightarrow CH_3COO^- + H^+$$

$$Step\ 2: CH_3COO^- \rightarrow CH_3COO\cdot + e^- \rightarrow \cdot CH_3 + CO_2$$

$$Step\ 3: 2 \times CH_3 \cdot \rightarrow C_2H_6$$

The adsorption and Kolbe oxidation of acetic acid on RuO_2/TiO_2 is presented in **Fig. S15a**. The region of 3500-3900 cm^{-1} (**Fig. S15b**) with weak signals is assigned to the vibration of free O-H or weak hydrogen bond (ν(O-H)) of molecular CH_3COOH, H_2O and surface hydroxyl groups (M-OH).[12] It can be observed that with increasing applied potential (0–10 V vs. Ag/AgCl), these peaks gradually diminish in intensity and eventually flatten. This is because as Kolbe electrolysis proceeds, acetic acid (CH_3COOH) is consumed, reducing the availability of H-bond donors (Step 1). Simultaneously, we observed a red shift from 3150 cm^{-1} to 3045 cm^{-1} and then shift back to 3070 cm^{-1} as the potential increases (**Fig. S15c**), and this broad peak gets stronger and then fades away. This might be due to the decarboxylation ($CH_3COO^- \rightarrow \cdot CH_3 + CO_2$), weakening O–H···O hydrogen bonds (step 2). And the produced intermediates like $\cdot CH_3COO^-$ or $\cdot CH_3$ radicals adsorb on RuO_2, disrupting the original H-bond network. The results

of the differential spectral analysis corroborate this viewpoint, as shown in **Fig. S15d**. An increasing signal at 2970 cm^{-1} that belong to $\nu(CH_3)$ of C_2H_6 was observed (Step 3)[13] additionally, transient peaks at 3030 and 2940 cm^{-1} suggest the involvement of methyl radical ($\cdot CH_3$) intermediates.[14] . The presence of $\cdot CH_3$ was also confirmed with our spin-trap reagent-added electrolysis shown later. Also, the change of CO_2 signal at 2340 and 2360 cm^{-1} suggests that CO_2 is rapidly generated and accumulated from 0-2V, which is consistent with the Kolbe decarboxylation reaction (Step 2), where the generated CO_2 saturates the interface and escapes as bubbles. Moreover, the signal at 1720 cm-1 assigned to the carbonyl group vibration ν(C=O) of acetic acid, 1610 and 1550 cm-1 belong to the anti-symmetric vibration of acetate ν(C-C-O) were also observed, their signal intensities both increased and then decreased, attributed to the adsorption of acetic acid on the electrode surface followed by gradual consumption (**Fig. S15e**).[15] Additionally, characteristic signals belong to adsorbed acetate were also detected. As shown in Fig. S15e,1260 cm^{-1} corresponds to the C-O vibration of adsorbed state acetate (CH_3COO^-), 1290 cm^{-1} to the symmetric deformation vibration of CH_3 (δ_s CH_3) 1200 cm^{-1} to the symmetric stretching vibration of COO- (ν_s COO^-), 1170 cm^{-1} corresponds to C-C-O stretching vibration[16] Their signal changes are also generally consistent with the process of the Kolbe reaction. Moreover, the observation of 1050 cm^{-1} corresponds to C-O stretching vibration might due to the formation of methanol. Overall, based on the *in-situ* ATR-FTIR technique, we verified the Kolbe oxidation process based on 3 steps as described above. Furthermore, to confirm the methyl radical formation during the reaction, we also conducted a radical-trapping control experiment by using TEMPO when running Kolbe oxidation.

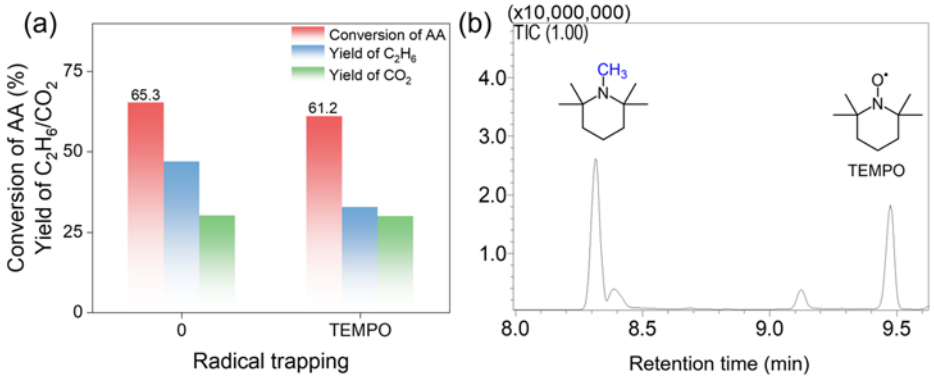

Fig. S16. (a) Obtained KBE reaction result by radcial-trapping control experiment, (b) TIC (Total Ion Chromatography) of the TEMPO-trapped molecule.

Based on the results, we found that the addition of TEMPO did not significantly affect the conversion of acetic acid (<5%) or the CO_2 yield, but the yield of ethane was significantly reduced, and we also found evidence of the capture of methyl radicals based on GC-MS analysis. This result confirms the decarboxylation step outlined in step 2 still occurred in the presence of TEMPO, but the resulting $\cdot CH_3$ was trapped by TEMPO reagent, which diminished the C_2H_6 yield. The trapped spin-trapped product, e.g. methylated TEMPO, was also detected in GC-MS.

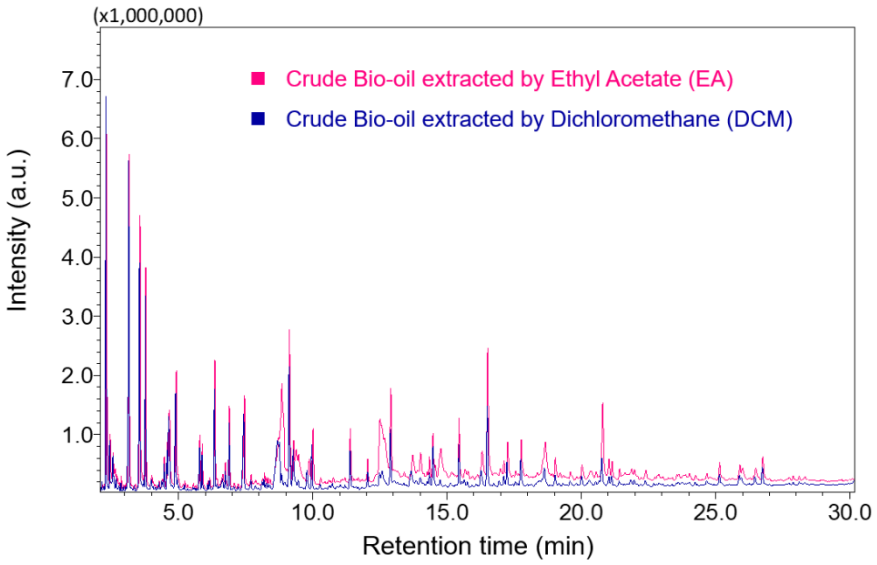

Fig. S17. TIC (Total Ion Chromatography) of crude bio-oil extracted by EA and DCM.

Table S6. GC/MS chromatogram major compounds in the crude bio-oil.

Item	Retention time (min)	Chemical	Similarity (%)
1	0.96	Methanol	98
2	1.04	Acetone	98
3	1.09	Methyl acetate	97
4	1.55	Hydroxy acetone	96
5	1.99	Propanoic acid	96
6	2.03	4-Methyl-2-pentanol	89
7	2.31	1-Hydroxy-2-butanone	98
8	2.45	Succi dialdehyde	91
9	2.56	Cyclopentanone	93
10	2.66	Butanoic acid	91
11	2.96	1-Hydroxy-3-methyl-2-butanone	90
12	3.16	**Furfural**	90
13	3.56	2-Furanmethanol	95
14	3.78	Acetoxy acetone	98
15	4.01	Dihydro-2H- pyran-3(4H)-one	88
16	4.06	4-Cyclopentene-1,3-dione	81
17	4.28	4-Hydroxy-3-hexanone	83
18	4.47	2-Cyclopenten-1-one	90
19	4.58	2-Acetylfuran	93
20	4.65	Gamma butyrolactone	95
21	4.92	Cyclohexanone	88
22	5.01	2-Cyclohexen-1-one	88
23	5.23	5-Methyl-2(5H)-furanone	91

24	5.34	3-Methyl-2,5-furandione	83
25	5.56	2,3-Dimethyl-1-pentanol	76
26	5.61	2-Hydroxy-gamma-butyrolactone	77
27	5.69	3-Methyl-4(3H)-pyrimidinone	73
28	5.79	4-Methyl-1-penten-3-ol	78
29	5.89	2-Oxo-butyl acetate	97
30	6.11	Methyl 2-furoate	93
31	6.16	3-Methyl-2(5H)-furanone	95
32	6.35	**Phenol**	98
33	6.52	3,4-Dimethylcyclopent-2-en-1-one	91
34	6.74	2,5-Dihydro-3,5-dimethyl-2-furanone,	93
35	6.89	Tetrahydrofurfuryl alcohol	92
36	7.45	3-Methyl-1,2-cyclopentanedione	96
37	7.71	2,3-Dimethyl-2-cyclopenten-1-one	91
38	7.88	4-Methyl-5H-furan-2-one	93
39	8.13	Tetrahydro-3,6-dimethyl-2H-pyran-2-one	83
40	8.20	3-Ethyl-2-hydroxy-2-cyclopenten-1-one	86
41	8.25	2-Methyl-phenol	95
42	8.33	3,4-Hexanedione	88
43	8.42	2-Acetylfuran	82
44	8.72	Allyl butyrate	88
45	8.86	2-Oxo-n-valeric acid	89
46	9.13	**Guaiacol**	96
47	9.29	4,5-Dimethyl-4-hexen-3-one	89
48	9.38	Cyclobutanol	85
49	9.87	3-Hydroxy-2-methyl-4H-pyran-4-one	94
50	10.01	3-Ethyl-2-hydroxy-2-cyclopenten-1-one	95
51	10.29	l, 4-(1-methylethyl)-cyclohexano	75
52	11.39	3-Ethyl-phenol	97
53	12.04	Creosol	96
54	12.5	**Catechol**	90
55	12.91	**2,3-Dihydrobenzofuran**	92
56	13.72	Glyceryl alpha-monoacetate	90
57	14.01	3-Methoxy-1,2-benzenediol	96
58	14.35	1-(2,5-Dihydroxyphenyl)-ethanone	92
59	14.48	4-Ethyl-2-methoxy- phenol	92
60	14.77	Hydroquinone	86
61	15.45	2-Methoxy-4-vinylphenol	93
62	16.52	**2,6-Dimethoxy-phenol**	92
63	16.99	4-Hydroxy-benzaldehyde	96
64	17.76	Vanillin	96

65	18.66	Hexahydro-1,8(2H,5H)-naphthalenedione,	79
66	19.03	3,5-Dimethoxy-4-hydroxytoluene	82
67	19.21	3-Methoxy-2-methyl-phenol	81
68	20.03	2- Hydroxy-6-methoxyacetophenone	78
69	20.79	2H-1-Benzopyran-2-one, 3,4-dihydro-6-hydroxy-	81
70	21.03	5-Tert-butylpyrogallol	78
71	21.15	2-Propanone, 1-(4-hydroxy-3-methoxyphenyl)-	91
72	21.42	6-Methoxychroman-2-one	75
73	21.98	4-ethenyl-2,6-dimethoxy-phenol	85
74	22.4	Methyl 3-(4-hydroxyphenyl) propionate	85
75	24.68	Methyl 3-(4-hydroxy-3-methoxyphenyl) propanoate	90
76	25.15	(E)-2,6-Dimethoxy-4-(prop-1-en-1-yl) phenol	92
77	25.9	1-(4-Hydroxy-3,5-dimethoxyphenyl)-ethanone	93
78	26.01	2-Propanone, 1-hydroxy-3-(4-hydroxy-3-methoxyphenyl)-	85
79	26.49	4-Methyldaphnetin	70
80	26.76	Syringylacetone	96
81	27.89	1-(4-Hydroxy-3,5-dimethoxyphenyl)- 1-propanone	87
82	28.12	3-(4-Hydroxy-3-methoxyphenyl)-2-propenoic acid	90
83	30.57	n-Hexadecanoic acid	94

These compounds are identified by comparing the mass spectra with the NIST17-1 library.

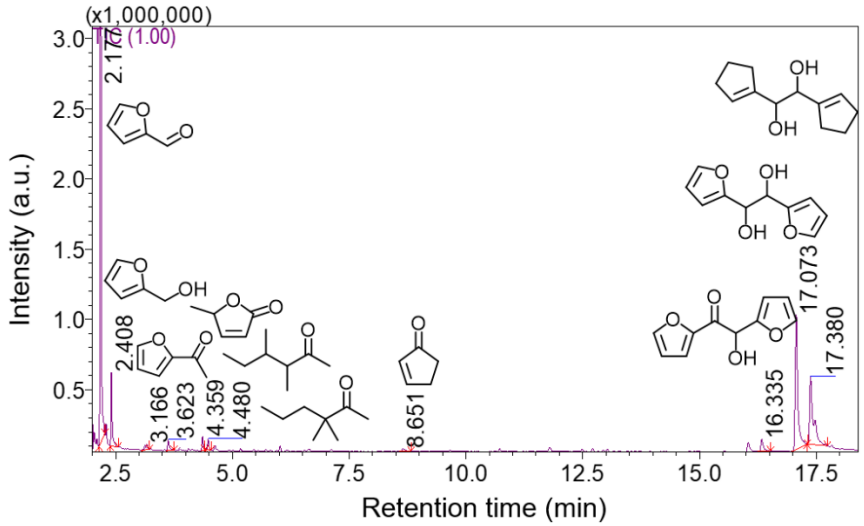

Fig. S18. TIC (Total Ion Chromatography) of KBE in the presence of furfural.

Table S7. GC/MS chromatogram analysis of major products after KBE in the presence of furfural.

Item	Retention time (min)	Chemicals detected after KBE	Similarity (%)
1	2.177	Furfural	97
2	2.408	Furfuryl alcohol	95
3	3.166	2-Acetylfuran	93
4	3.623	*β*-Angelica lactone	96
5	4.359	3,3-Dimethyl-2-hexanone	89
6	4.480	3,4-Dimethyl-2-hexanone	88
7	8.651	2-Cyclopenten-1-one	87
8	16.34	2,2-Furoin	87
9	17.073	1,2-Bis(2-furanyl)ethane-1,2-diol	88
109	17.380	1,2-Di(1-cyclopentenyl)-1,2-ethanediol	87

These compounds are identified by comparing the mass spectra with the NIST17-1 library.

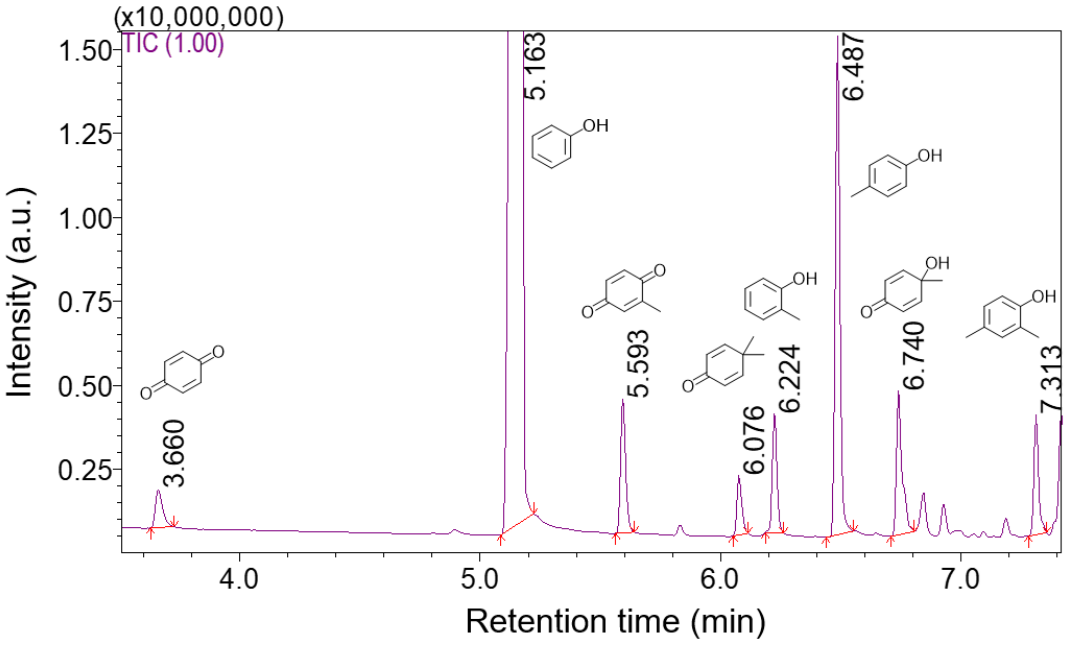

Fig. S19. TIC (Total Ion Chromatography) of KBE in the presence of phenol.

Table S6. GC/MS chromatogram analysis of major products after KBE in the presence of phenol.

Item	Retention time (min)	Chemicals detected after KBE	Similarity (%)
1	3.660	*p*-benzoquinone	98
2	5.163	Phenol	93
3	5.593	2-Methyl-*p*-benzoquinone	97
4	6.076	4,4-Dimethylcyclohexadienone	94
5	6.224	2-Methylphenol	98
6	6.487	*p*-Cresol	98
7	6.740	4-Hydroxy-4-methylcyclohexa-2,5-dien-1-one	84
8	7.313	2,4-Dimethylphenol	98

These compounds are identified by comparing the mass spectra with the NIST17-1 library.

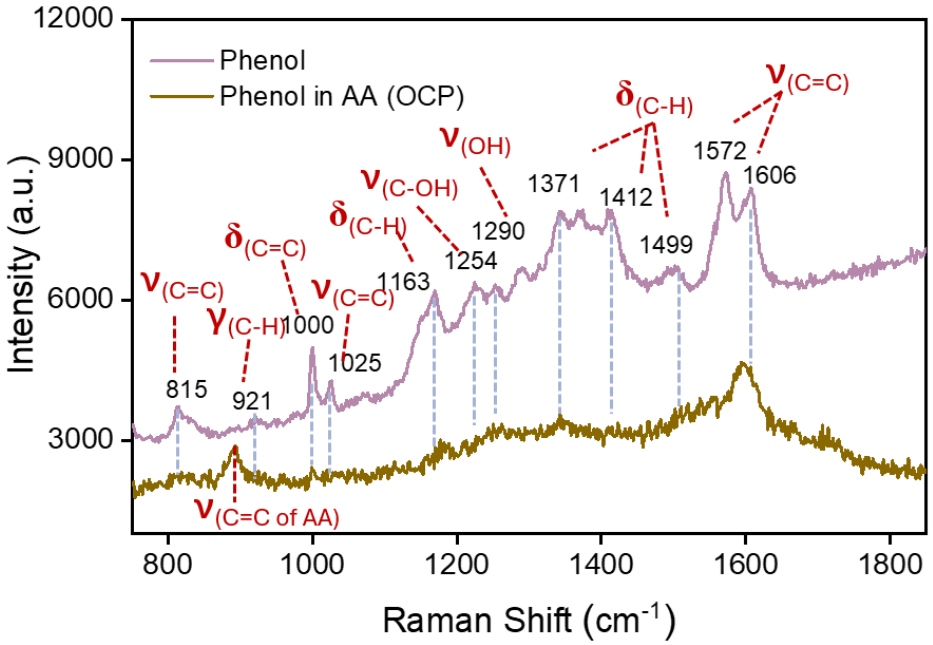

Fig. S20. Raman spectra of pure phenol and 100 mM phenol in AA.

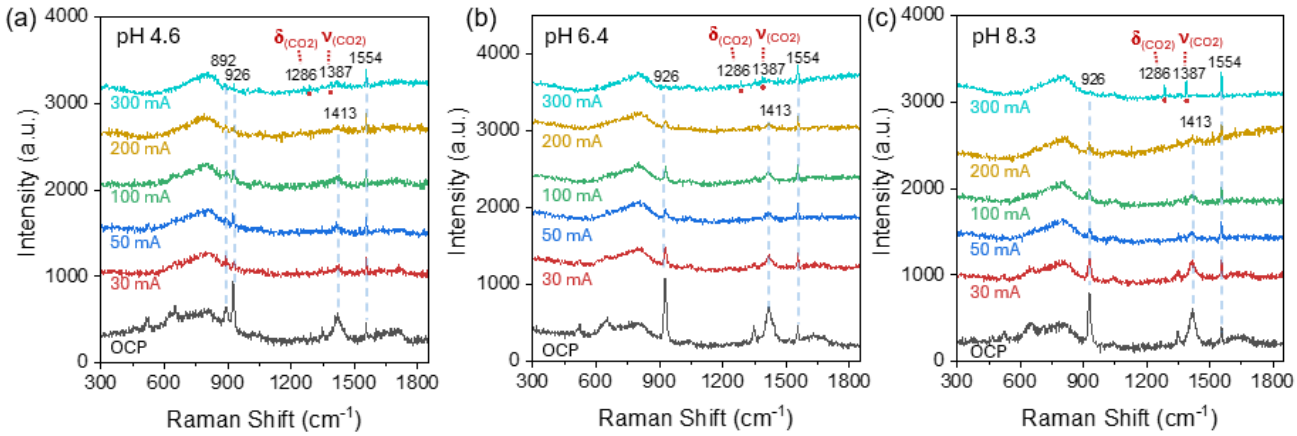

Fig. S21. *In-situ* Raman signal variation of 1.0M AA with different currents in various pH.

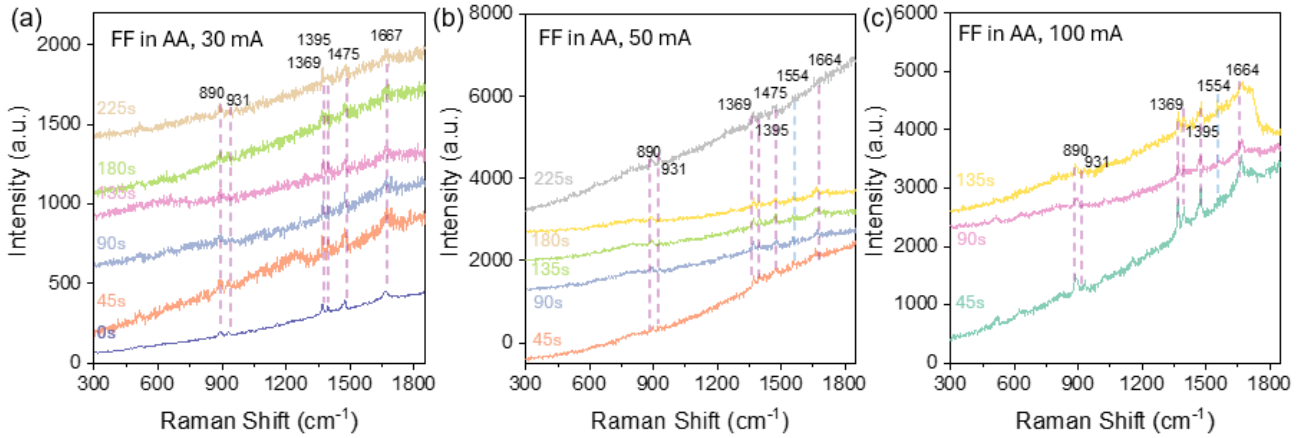

Fig. S22. *In-situ* Raman signal variation of FF in 1.0M AA with different currents with time.

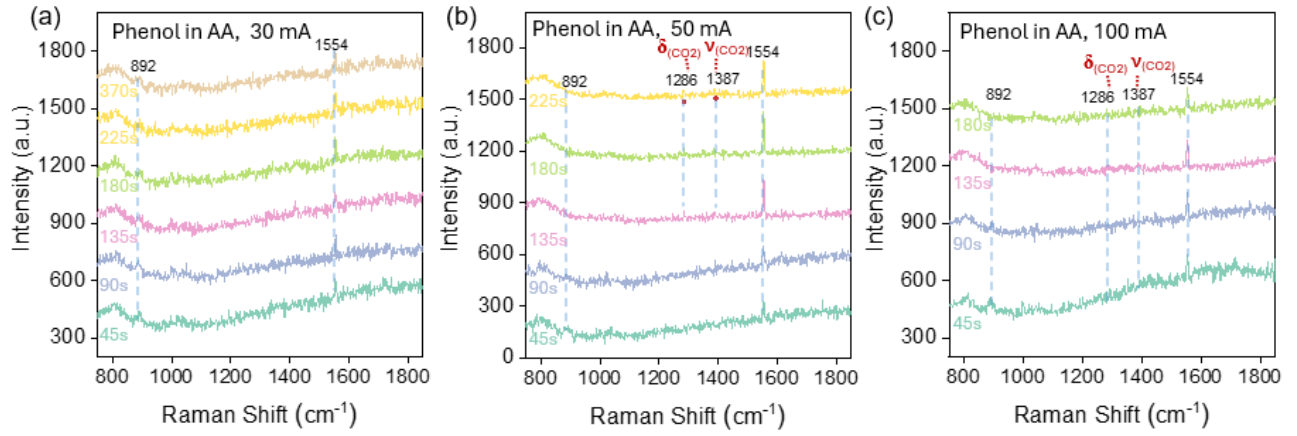

Fig. S23. *In-situ* Raman signal variation of phenol in 1.0 M AA with different currents with time.

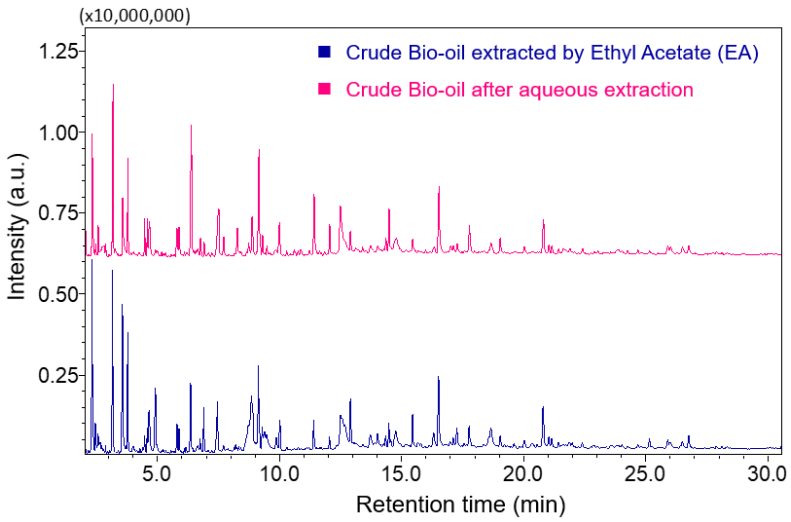

Fig. S24. TIC (total ion chromatogram) of crude bio-oil extracted by EA and aqueous-extracted bio-oil.

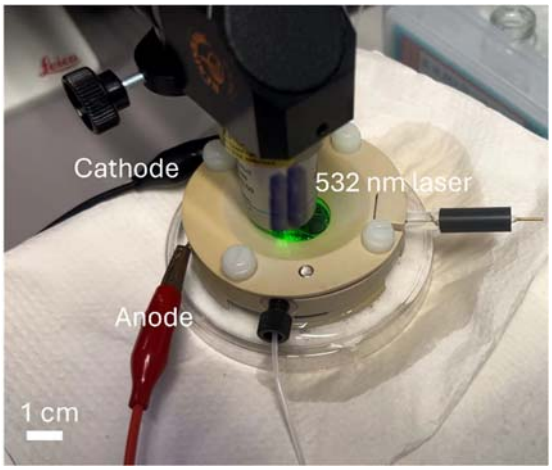

Fig. S25. Scheme of the *in-situ* Raman measurement.

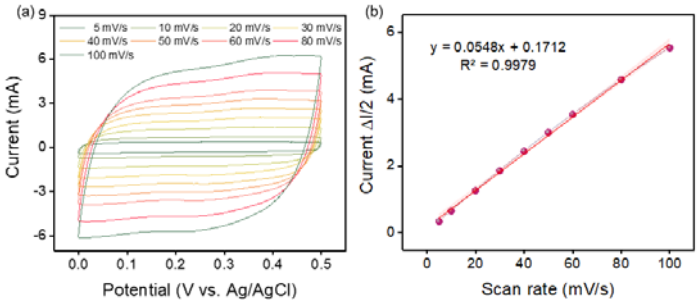

Fig. S26. (a) Voltammetry characteristic curves recorded with different sweep velocity using Ag/AgCl as the reference electrode. (b) Diagram of ΔI/2 vs. sweep velocity. The electrochemically active surface areas (ECSA) were estimated from the electrochemical double-layer capacitance (C_{dl}) of the catalytic surface. The C_{dl} was determined by plotting the ΔI/2 ($\Delta I = I_a - I_c$, where I_a is the anodic current and I_c is the cathodic current at the middle voltage) against the scan rate, where the slope is equal to Cdl. The specific capacitance Cs= 40 μF cm^{-2} is used[17], and the ECSA is calculated according to $ECSA = C_{dl}/C_s$.

References

1. C. Urban, J. Xu, H. Sträuber, T. R. dos Santos Dantas, J. Mühlenberg, C. Härtig, L. T. Angenent and F. Harnisch, *Energ. Environ. Sci.*, 2017, **10**, 2231-2244.
2. Y. Peng, Y. Ning, X. Ma, Y. Zhu, S. Yang, B. Su, K. Liu and L. Jiang, *Adv. Func. Mater.*, 2018, **28**, 1800712.
3. J. Meyers, N. Kurig, C. Gohlke, M. Valeske, S. Panitz, F. J. Holzhäuser and R. Palkovits, *ChemElectroChem*, 2020, **7**, 4873-4878.
4. G. Yuan, L. Wang, X. Zhang, R. Luque and Q. Wang, *ACS Sustain. Chem. Eng.*, 2019, **7**, 18061-18066.
5. C. Taube, A. Fischer and M. Beyer, *ChemCatChem*, 2024, **16**, e202400628.
6. N. Baumgarten, B. J. Etzold, P. Löb, J. Magomajew and A. Ziogas, *Chem. Ing. Tech.*, 2024, **96**, 789-800.
7. K. Neubert, M. Schmidt and F. Harnisch, *ChemSusChem*, 2021, **14**, 3097-3109.
8. N. Ahad and A. de Klerk, *Fuel*, 2018, **211**, 415-419.
9. Y. Qiu, J. A. Lopez-Ruiz, G. Zhu, M. H. Engelhard, O. Y. Gutiérrez and J. D. Holladay, *Appl. Catal. B*, 2022, **305**, 121060.
10. Y. Qiu, J. A. Lopez-Ruiz, U. Sanyal, E. Andrews, O. Y. Gutiérrez and J. D. Holladay, *Appl. Catal. B: Environ.*, 2020, **277**, 119277.
11. S. F. Shams, M. Kashefi and C. Schmitz-Antoniak, *New J. Chem.*, 2018, **42**, 3050-3062.
12. M. Hasan, M. Zaki and L. Pasupulety, *Appl. Catal. A*, 2003, **243**, 81-92.
13. E. Kovalev, A. Shalygin, A. Shubin, I. Kozhevnikov, S. Prikhod'ko, N. Y. Adonin, S. Kazarian and O. Martyanov, *J. Mol. Liquids*, 2022, **348**, 118082.
14. M. J. Abplanalp and R. I. Kaiser, *Astrophys. J.*, 2016, **827**, 132.
15. M. Heinen, Z. Jusys and R. J. Behm, *J. Phys. Chem. C*, 2010, **114**, 9850-9864.
16. S. Beyhan, J.-M. Léger and F. Kadırgan, *Appl. Surf. Sci.*, 2014, **321**, 426-431.
17. Y. Qin, T. Yu, S. Deng, X.-Y. Zhou, D. Lin, Q. Zhang, Z. Jin, D. Zhang, Y.-B. He and H.-J. Qiu, *Nat. Commun.*, 2022, **13**, 3784.